

## Electrocatalysis

# Electronic Modulation and Active Site Exposure Using C<sub>60</sub> Fullerenolamine Enable High-Performance Alcohol Oxidation on Pd Metallene Catalysts

Shuqian Xie<sup>+</sup>, Jiashuo Fu<sup>+</sup>, Qi Huang, Wenhao Yang, Ao Yu, Yingying Yan, Zengyuan Li, Ping Peng, Yajun Yin, Haining Wang, Luis Echegoyen, and Fang-Fang Li\*

**Abstract:** The availability of active sites and the electronic structure of metal heterogeneous catalysts are crucial to maximize their catalytic performance. In this study, we describe a new and efficient catalyst system, C<sub>60</sub> fullerenolamine (FA)-modified Pd metallene (Pdene), and demonstrate that the FA molecules not only increase the active sites availability but also exert an electronic effect that enhances the catalytic performance of Pdene in alcohol oxidation reactions. Specifically, FA increases the electrochemical active surface area through dispersion, while its electron-withdrawing characteristics induce an electron-deficient surface on Pdene, which facilitates the adsorption of electron-rich intermediates (OH\*) and the desorption of electron-deficient poisonous intermediates (CO\*). The practical significance of this modification is demonstrated by achieving a 54.5% increase in mass activity and 46.3% enhancement in specific activity for ethanol oxidation relative to Pdene. Beyond these improvements, the FA-Pdene catalyst demonstrates exceptional operational stability, superior CO poisoning resistance, and enhanced C1 pathway selectivity. An in-depth analysis utilizing in-situ Fourier transform infrared spectroscopy, coupled with density functional theory calculations, offers valuable insights into how the FA ligand modulates the mechanistic pathways involved in ethanol oxidation processes. This fullerene-mediated catalytic effect could hold the key to unlocking the potential of the metal-based system.

## Introduction

The rapid consumption of fossil fuels and the resulting degradation of the environment have sparked a drive to develop efficient electrochemical energy conversion technologies. Direct alcohol fuel cells (DAFCs) have garnered considerable attention owing to their high energy densities, ease of storage and transportation, as well as the widespread availability of raw materials.<sup>[1]</sup> Despite their promise as fuel sources, the electrooxidation process of alcohols presents significant challenges due to the sluggish kinetics resulting from the complex multi-electron transfer processes involved. Palladium (Pd)-based catalysts have exhibited significant

promise in boosting alkaline electrochemical alcohol oxidation, however, their catalytic activity and stability have been constrained by factors such as a low density of active sites, unsuitable electronic properties, and susceptibility to poisoning.<sup>[2,3]</sup> These challenges underscore the urgent need to design and fabricate highly active and poisoning-resistant catalysts that can efficiently catalyze the oxidation of alcohols.

The emerging two-dimensional (2D) metallenes present a promising solution through their unique structural advantages.<sup>[4,5]</sup> For example, metallene exhibits a high specific surface area, high atomic utilization and remarkable unsaturated metal sites, which can provide more active sites for catalytic reactions, thereby significantly enhancing catalytic activity.<sup>[6]</sup> However, the high surface energy of metallenes renders them susceptible to interlayer stacking during catalytic reactions, leading to a substantial loss of active sites and subsequent performance degradation.<sup>[7]</sup> Consequently, to enhance the catalytic performance of metallenes, two complementary strategies need to be adopted: 1) achieving high dispersion of metallenes to maximize active site availability, and 2) engineering the electronic properties of metallenes through advanced material design to achieve optimal catalytic properties. Notably, strategies such as defect engineering, interface engineering, pore engineering, doping, and alloying have been successfully utilized to either enhance the density of active sites or modulate the electronic structures of metallenes. These optimizations have markedly improved their catalytic performance in reactions such as hydrogen

[\*] S. Xie<sup>+</sup>, Q. Huang, W. Yang, A. Yu, Y. Yan, Z. Li, P. Peng, Y. Yin, F.-F. Li  
State Key Laboratory of Materials Processing and Die & Mould Technology, School of Materials Science and Engineering, Huazhong University of Science and Technology, Wuhan 430074, P.R. China  
E-mail: ffl@hust.edu.cn

J. Fu<sup>+</sup>, H. Wang  
Beijing Key Laboratory of Bio-inspired Energy Materials and Devices, School of Energy and Power Engineering, Beihang University, Beijing 100191, P.R. China

L. Echegoyen  
Institut Català d'Investigació Química, Ave. Països Catalans 16, Tarragona 43007, Spain

[<sup>+</sup>] Both authors contributed equally to this work.

Additional supporting information can be found online in the Supporting Information section

evolution,<sup>[8,9]</sup> nitrate reduction,<sup>[10,11]</sup> oxygen reduction,<sup>[12,13]</sup> and alcohol oxidation reactions.<sup>[14]</sup> Nevertheless, the strategic application of ligand modification to enhance the catalytic activity and stability of metallenes, particularly for alcohol oxidation reactions, has received far less attention and remains largely unexplored.

Consequently, employing a post-modification approach, which is particularly beneficial due to its minimal impact on the morphology of Pd metallene (Pdene), to functionalize the Pdene surface with ligands presents significant potential for tailoring its electronic properties and gaining a more profound insight into the impact of ligands on catalytic performance. However, it is important to acknowledge that while attaching ligands to metal surfaces can induce unique electronic effects, such modifications will inevitably result in partial coverage of the metal surface. This in turn, reduces the number of active sites available and may hinder the access of reactants to the catalytic sites.<sup>[15,16]</sup> Therefore, considering the critical importance of surface site availability and electronic properties, developing ligands that integrate these properties presents a promising approach to enhance catalytic performance, although it is a significant challenge.

Fullerenes and their derivatives, as spherical molecular carbon with  $\pi$ -conjugated surfaces, possess exceptional abilities in electron buffering and charge transportation, offering significant potential to exert electronic effects on heterogeneous metal catalysts. For example,  $C_{60}$  fullerene is capable of stabilizing the metastable active  $Cu^+$  species in a  $Cu/SiO_2$  catalyst through electron donation-acceptance interactions, facilitating the ambient-pressure hydrogenation of dimethyl oxalate to ethylene glycol.<sup>[17]</sup> Depositing a  $C_{60}$  layer onto the transition metal substrates balances the electron density at catalytic transition metal sites, promoting the activation of nitrogen for ammonia synthesis.<sup>[18]</sup> Loading Pt/Ru sites onto  $C_{60}$  or hydroxylated  $C_{60}$  can enhance their hydrogen evolution performance, with  $C_{60}$  playing a crucial role in regulating the electron density of the metal catalytic sites.<sup>[19–22]</sup> In light of this, employing fullerenes as ligands for the surface engineering of metallene has the potential for tuning the interactions between metal active sites and reaction intermediates in alcohol oxidation reactions.

In this article, we describe the creation of a fullerene-amine (FA)-modified Pd metallene catalyst (FA-Pdene), which exhibits enhanced activity, stability, CO resistance, and C1 selectivity for ethanol oxidation reactions. The FA modification not only increases the availability of active sites but also creates electron-deficient Pd surfaces. Such an electronic state favors the adsorption of electron-rich intermediates ( $OH^*$ ) while disfavoring the adsorption of electron-deficient poisonous intermediate ( $CO^*$ ), thereby significantly boosting the catalytic performance of FA-Pdene for the oxidation of ethanol, methanol and ethylene glycol. This work not only highlights the potential of fullerene modifiers in promoting alcohol oxidation reactions but also opens a new avenue for the surface modification of metallenes.

## Results and discussion

### Synthesis and Characterization of FA-Pdene

FA-Pdene was prepared through a simple two-step process (Figure 1a). In brief, the reaction between  $Pd(acac)_2$  and  $W(CO)_6$  (acting as a reducing and structure-directing agent) resulted in the formation of Pdene under moderate reduction conditions at 50 °C.<sup>[12]</sup> Then, fullerene-amine (FA), featuring multiple amine ( $NH_2$ ) and hydroxyl ( $OH$ ) groups attached to the  $C_{60}$  cage,<sup>[23]</sup> was introduced to the aqueous dispersion of Pdene while stirring (Figure 1a). During this process, the Pdene coordinated with the FA molecules, leading to the formation of FA-modified Pdene catalysts (FA-Pdene). Considering the presence of both  $-NH_2$  and  $-OH$  groups on  $C_{60}$ , we performed a control experiment to explore which group is primarily responsible for the interaction between Pdene and  $C_{60}$ . Thus,  $C_{60}(OH)_{24}$  was also synthesized<sup>[24]</sup> and utilized in lieu of FA to synthesize  $C_{60}(OH)_{24}$ -Pdene, following the same procedures that were implemented for the preparation of FA-Pdene. As depicted in Figure S1a,  $C_{60}(OH)_{24}$ -Pdene exhibited significant precipitation after 2 h. By the end of a 12 h period, the precipitate had completely settled to the bottom, leaving the supernatant with the distinctive brown color of  $C_{60}(OH)_{24}$ . This observation suggests that  $C_{60}(OH)_{24}$  does not effectively interact with Pdene, as indicated by the comparable electrochemical surface area (ECSA) (Figure S1b,c). This experiment shows the importance of the  $-NH_2$  groups to modify the surface of Pdene. For controlled comparison, an organic fatty amine with electron-donating properties, namely ethylenediamine (EDA) was also selected to modify Pdene. EDA-Pdene was synthesized using the same procedure.

Once FA is added to the Pdene dispersion, the solution displays remarkable dispersibility which can be clearly observed with the naked eye, signifying a strong interaction between FA and the Pdene surface. Moreover, the presence of FA enhances the stability of FA-Pdene, allowing it to maintain excellent dispersibility even after being stored for 12 h. In contrast, Pdene and EDA-Pdene exhibit significant sedimentation (Figure S2). Good dispersibility is advantageous as it exposes more of the Pdene surface area, maximizing the availability of catalytic sites, and consequently improving the catalytic activity.

The morphologies and microstructures of the prepared Pdene and FA-Pdene were characterized by transmission electron microscopy (TEM). As shown in Figures 1b and S3, they both display a wrinkled 2D nanosheet structure. The post-synthesis approach (e.g., adding FA subsequent to the synthesis of Pdene) employed for FA-Pdene has little effect on their morphology. As shown in Figure 1c–e, the HR-TEM images of FA-Pdene reveal the coexistence of crystalline and amorphous domains within the layer, and the dominant exposed surface in the crystalline domain is the Pd (111) facet, characterized by a lattice spacing of 0.22 nm (Figure 1e). These results are in agreement with the observations recorded for Pdene in Figure S3d, further indicating that there is very

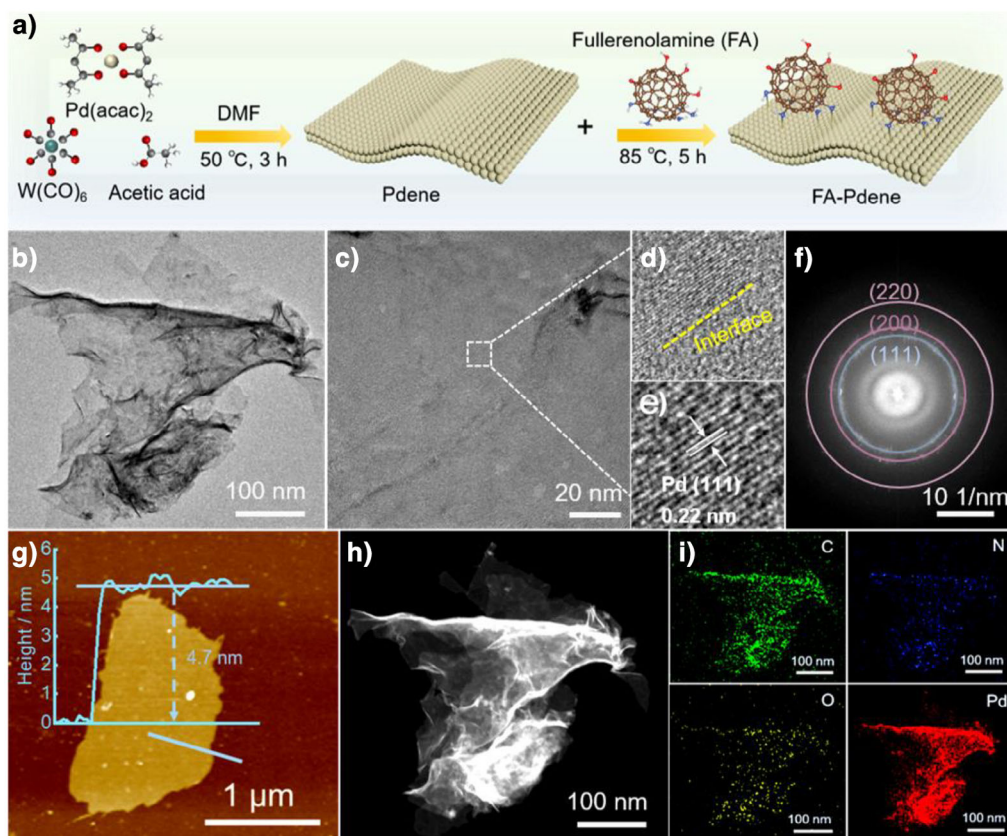


**Figure 1.** a) Schematic representation of the synthesis of FA-Pdene. Bright-field b) TEM and c) HRTEM images of FA-Pdene. d), e) Enlarged selected area in (c). f) SAED pattern and g) AFM image of FA-Pdene. h) Dark-field TEM image and i) the associated EDX elemental mappings of FA-Pdene. Note: The functionalization positions of  $\text{NH}_2$  and  $\text{OH}$  groups on  $\text{C}_{60}$  were selected arbitrarily, and a wide variety of isomeric FA compounds is present.

little impact on the Pdene structure following the incorporation of FA. Notably, the crystalline/amorphous hetero-phases can provide rich interfaces and facilitate the generation of catalytic active sites, such as unsaturated coordinated sites, defects, and boundaries.<sup>[12]</sup> The selected-area electron diffraction (SAED) pattern of FA-Pdene (Figure 1f) displays three diffraction rings due to the coexistence of crystalline and amorphous regions, indicating the polycrystalline nature of FA-Pdene. The diffraction rings correspond to Pd (111), (200), and (220) crystal faces in sequence from the center of the ring toward the outside. The AFM image of FA-Pdene exhibits a thickness of 4.7 nm (Figure 1g), which is 1.3 nm larger than the thickness of Pdene (Figure S3b,c). This increase in thickness agrees perfectly well with the dimension of a single-layer of FA molecules. As confirmed by the high-angle annular dark field-scanning transmission electron microscopy (HAADF-STEM) image and its corresponding energy-dispersive X-ray (EDX) map (Figure 1h,i), the C, N, and O elements are evenly distributed over the surface of Pdene. This distribution verifies the successful attachment of FA onto the surface of Pdene, given that FA is mainly responsible for the elemental C/N/O content. The relative amounts of C, N, O, and Pd are 28.29, 1.42, 3.13 and 67.16 wt%, respectively (Figure S4 and Table S1).

Powder X-ray diffraction (PXRD) was conducted to investigate the crystalline structure characteristics of the catalysts (Figure 2a). In the XRD pattern of the comparison sample, Pd/C, the diffraction peaks corresponding to C (002), Pd (111), Pd (200), Pd (220), and Pd (311) (PDF # 46–1043) are observed. Pdene and FA-Pdene exhibit XRD patterns that are similar to that of Pd/C. By comparison, it can be found that the peak intensity of FA-Pdene decreases, which is attributed to the coverage with the non-crystalline FA on the surface of Pdene. The successful modification was further confirmed by Fourier transform infrared spectroscopy (FTIR) (Figure 2b). The spectrum of pure FA shows two broad peaks located around  $3426$  and  $3140\text{ cm}^{-1}$ , which are ascribed to stretching vibrations of O–H ( $\nu$  O–H) and N–H ( $\nu$  N–H) bonds, respectively. The intense absorption peak at  $1608\text{ cm}^{-1}$  is assigned to the stretching vibration of the C–O bond ( $\nu$  C–O), and the vibrations observed at  $1398$  and  $1105\text{ cm}^{-1}$  originate from scissoring vibrations of C–O–H ( $\delta_s$  C–O–H) and the stretching vibration of C–O ( $\nu$  C–O), respectively.<sup>[23]</sup> These spectral features confirm the successful attachment of amino ( $-\text{NH}_2$ ) and hydroxyl ( $-\text{OH}$ ) groups to  $\text{C}_{60}$ . In the spectrum of pure Pdene, no discernible absorption peaks are observed due to its metallic nature. In contrast, FA-Pdene exhibits distinct characteristic absorption peaks for FA at



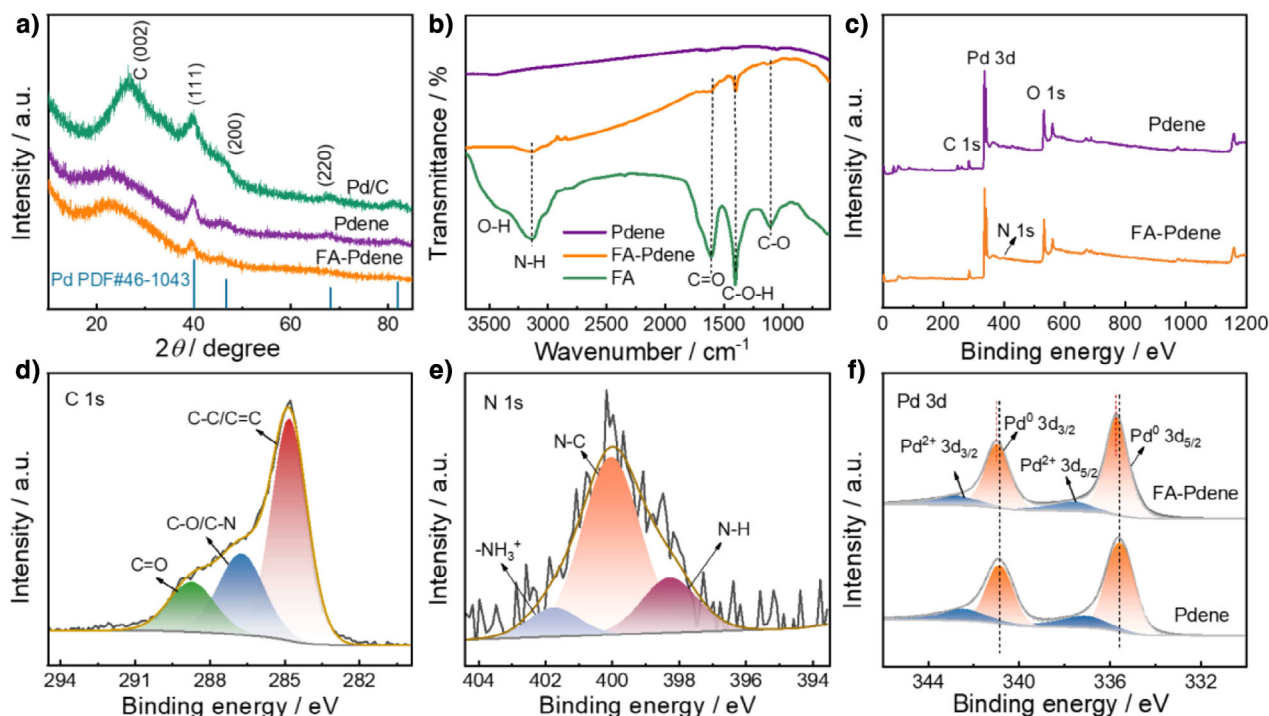


**Figure 2.** a) XRD patterns of commercial Pd/C, Pdene and FA-Pdene, and the standard XRD pattern of Pd. b) FTIR spectra of FA, Pdene and FA-Pdene. c) XPS scans for Pdene and FA-Pdene. High-resolution XPS spectra of d) C 1s and e) N 1s in FA-Pdene, and f) Pd 3d in Pdene and FA-Pdene.

3140, 1608, 1398, and 1105  $\text{cm}^{-1}$ , which offer compelling evidence for the successful modification of Pdene with FA.

The chemical composition and chemical states for the samples were studied by X-ray photoelectron spectroscopy (XPS). As shown in Figure 2c, the survey spectrum of FA-Pdene displays peaks at 284.8, 335.7, 400.0, and 532.5 eV, corresponding to the binding energies of C 1s, Pd 3d, N 1s and O 1s, respectively.<sup>[25]</sup> Notably, FA is the principal sources of the N element, therefore, the presence of the N element in the samples confirms the successful introduction of FA onto Pdene. The content of each element, calculated based on XPS analysis, is summarized in Table S2. In the high-resolution C 1s XPS spectra of FA-Pdene (Figure 2d), the peaks centered at 289.1, 287.8, 286.4, and 284.8 eV correspond to the binding energies of -COOH, C=O (C-N), C-O-C, and C-C (C=C), respectively. In the N 1s spectrum, peaks with binding energies of 401.8, 400.3, and 398.3 eV are ascribed to  $-\text{NH}_3^+$ , C-N (from the C-NH<sub>2</sub> group) and N-H (from the C-NH<sub>2</sub> group), respectively (Figure 2e).<sup>[23]</sup> The high resolution Pd 3d XPS spectra of Pdene and FA-Pdene reveal two pairs of well-defined peaks (Figure 2f). The red peaks correspond to Pd<sup>0</sup> 3d<sub>3/2</sub>/Pd<sup>0</sup> 3d<sub>5/2</sub>, due to the metallic state of Pd, while the blue peaks correspond to Pd<sup>2+</sup> 3d<sub>3/2</sub>/Pd<sup>2+</sup> 3d<sub>5/2</sub>, due to the oxidized Pd.<sup>[25]</sup> The observation of Pd<sup>2+</sup> in the XPS spectra is attributed to the surface oxidation of Pd. Compared with Pdene, the binding energy for Pd in FA-Pdene undergoes a shift of 0.2 eV toward higher binding energy, indicating a strong interaction between FA and Pdene, leading to charge transfer from Pdene to FA.

X-ray absorption near edge structure (XANES) spectra and Fourier transform extended X-ray absorption fine struc-

ture (FT-EXAFS) spectra were acquired to explore the local electronic structure and coordination environment of the Pd species in FA-Pdene. From the XANES spectra (Figure 3a), the Pd K-edge position for FA-Pdene is very close to that of the Pd foil, but far from that of the PdO reference. This indicates that the valence state of Pd in FA-Pdene is near to zero, consistent with the XPS results. The local chemical environment of Pd atoms in FA-Pdene was analyzed through FT-EXAFS (Figure 3b,c) and wavelet transform diagrams (Figure 3d-f). As shown in Figure 3b, the peaks located at 1.58 and 2.48 Å are associated with the Pd-N and Pd-Pd scattering pairs, respectively. Based on this observation, it can be deduced that FA and the Pdene substrate are bridged through N-atoms. In addition, the Pd-Pd distance (2.48 Å) in FA-Pdene is shorter than that for Pd foil (2.51 Å), implying a compressive strain induced by the 2D nature of the metallene.<sup>[26]</sup> According to the relevant FT-EXAFS spectrum of the Pd K-edge fitting results (Figure 3c), the coordination number for Pd-Pd and Pd-N in FA-Pdene are -6.2 and -2.5, respectively. In addition, the fitting results for the R space and K space for the Pd K-edge for a Pd foil and PdO are displayed in Figures S5, S6 and Table S3. A comparison of the wavelet transform diagram further confirms the presence of Pd-Pd and Pd-N bonds in FA-Pdene (Figure 3d-f).

### Electrocatalytic Alcohol Oxidation Performance

The electrochemical active surface area (ECSA), which is a critical factor in determining the catalyst's activity, was initially assessed by cyclic voltammetry curves (CVs) in

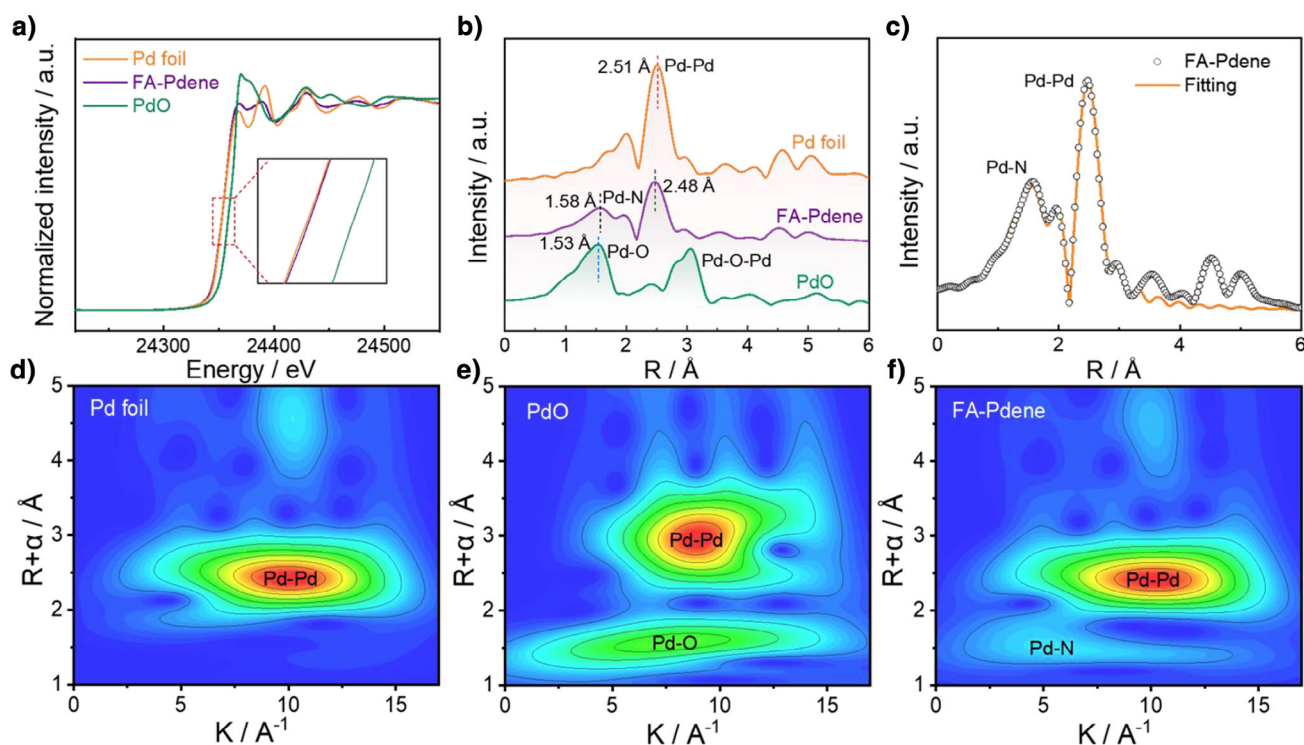


**Figure 3.** a) The normalized XANES spectra at the Pd K-edge and b) derived FT-EXAFS spectra for Pd foil, FA-Pdene and PdO. c) EXAFS fitting for FA-Pdene. d)–f) Wavelet transform for Pd K-edge data for Pd foil, FA-Pdene and PdO.

1.0 M KOH electrolyte. As displayed in Figure 4a, a distinct reduction peak appears between  $-0.50$  and  $-0.30$  V versus SCE for all the tested catalysts, signifying the reduction of PdO to Pd. Further comparison reveals that the PdO reduction peak of FA-Pdene, which occurs at  $-0.36$  V, is more positive compared to that of Pdene ( $-0.38$  V) and Pd/C ( $-0.40$  V). This positive shift implies that the oxygen species on the catalyst surface can be removed more easily, favoring the recovery of the Pd active sites.<sup>[27]</sup> The ECSA of the three catalysts was calculated by integrating the area of the PdO reduction peak, and the results are summarized in Figure 4b. It exhibits that FA-Pdene possesses the largest ECSA value ( $345.7 \text{ cm}^2 \text{ mg}_{\text{Pd}}^{-1}$ ), as compared with Pdene ( $325.9 \text{ cm}^2 \text{ mg}_{\text{Pd}}^{-1}$ ) and Pd/C ( $242.0 \text{ cm}^2 \text{ mg}_{\text{Pd}}^{-1}$ ). The incorporation of FA enhances ECSA by increasing the accessibility of active surface sites, instead of diminishing the active area through site coverage. This improvement primarily arises from the hydrophilic spherical FA molecules, which enable the Pdene to disperse well, effectively preventing the aggregation of 2D Pd nanosheets and maximizing the exposure of the catalytically active surfaces.

The electrocatalytic ethanol oxidation reaction (EOR) properties of the catalysts were evaluated in 1.0 M KOH + 1.0 M ethanol solution. Initially, the impact of the FA dosage on activity was examined through CV experiments. The results reveal that FA-Pdene synthesized with 4 mg of FA exhibits a higher ECSA and superior performance compared to FA-Pdene synthesized using 2 or 6 mg of FA (Figure S7). This finding indicates that FA addition amount is crucial to achieve a balance between maximizing accessible

active sites and optimizing the electronic properties of Pd.

As compared in Figure 4c, FA-Pdene (note: unless otherwise specified, FA-Pdene refers to the sample prepared with 4 mg of FA) delivers a higher forward peak current density (resulting from the oxidation of adsorbed ethanol species) than Pdene and Pd/C. In addition, the onset oxidation potential of ethanol ( $E_{\text{ethanol, o}}$ ) for FA-Pdene shifts negatively by 36 and 106 mV as compared with Pdene and Pd/C catalysts, respectively, showing that FA-Pdene exhibits the highest activity for EOR (Figure S8). To assess the intrinsic activity of the catalysts, the oxidative current in the forward scan was normalized by the mass loading of Pd and the ECSA on the electrode to obtain the mass activity and specific activity, respectively. The results presented in Figure 4d shows that FA-Pdene exhibits a mass activity of  $4123.0 \text{ mA mg}_{\text{Pd}}^{-1}$ , which is 1.5 and 7.1 folds higher than that of Pdene ( $2669.2 \text{ mA mg}_{\text{Pd}}^{-1}$ ) and commercial Pd/C ( $583.0 \text{ mA mg}_{\text{Pd}}^{-1}$ ). Therefore, the FA ligand enhances the mass activity of Pdene by 54.5%. Moreover, FA-Pdene also demonstrates a higher specific activity of  $12.0 \text{ mA cm}_{\text{Pd}}^{-2}$ , significantly surpassing Pdene ( $8.2 \text{ mA cm}_{\text{Pd}}^{-2}$ ) and commercial Pd/C ( $2.3 \text{ mA cm}_{\text{Pd}}^{-2}$ ). Impressively, in comparison with the advanced EOR electrocatalysts reported recently, the mass activity and specific activity of FA-Pdene are quite remarkable (Figure 4j).<sup>[25,28–36]</sup>

To further evaluate the EOR kinetics, electrochemical impedance spectroscopy (EIS) was measured in a solution containing 1.0 M KOH and 1.0 M ethanol. Figure 4e exhibits the Nyquist plots obtained from EIS for the four catalysts.

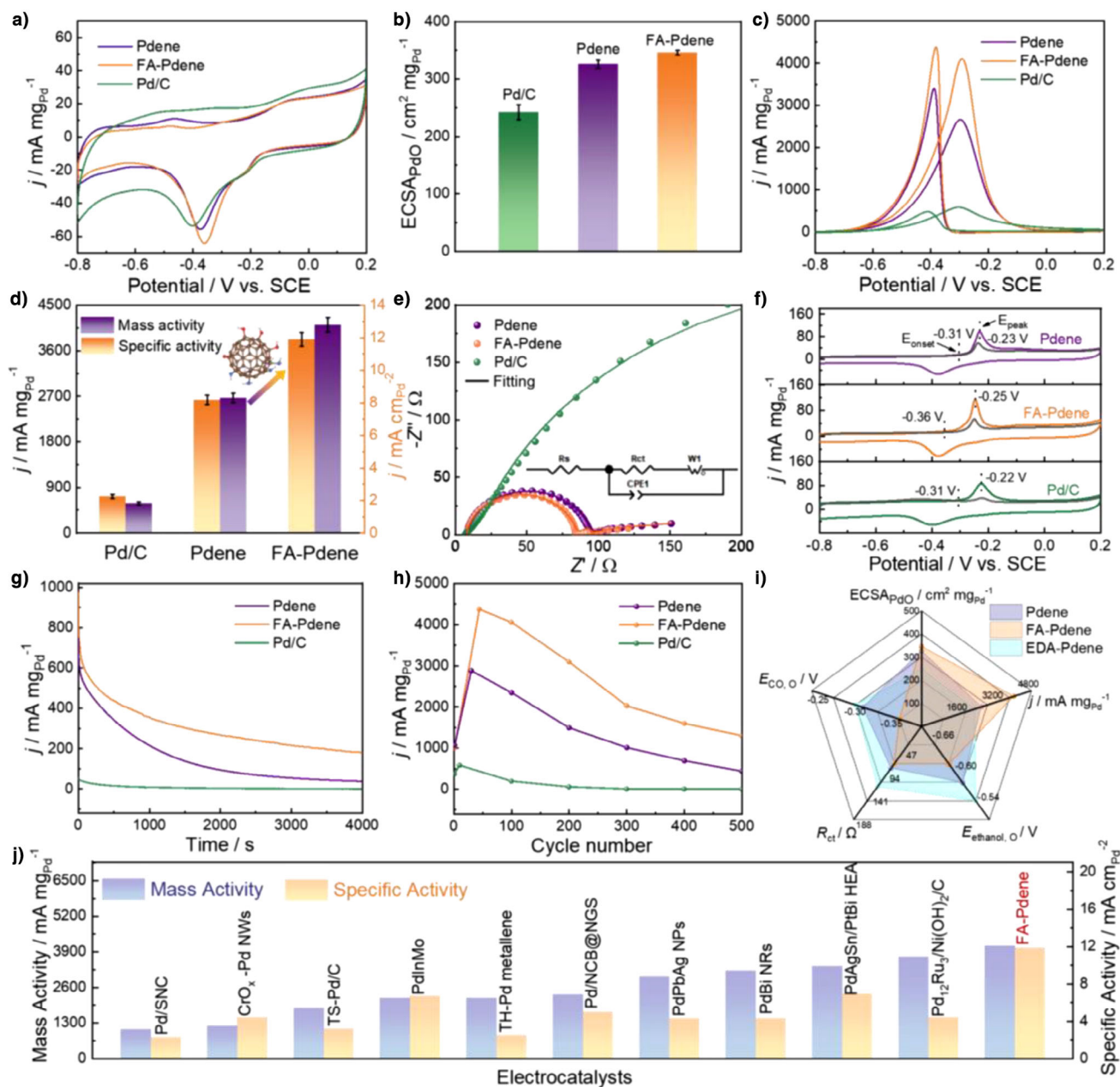


**Figure 4.** a) CVs of the catalysts in 1.0 M KOH. b) ECSAs derived from PdO reduction peaks in CVs. Error bars represent  $\pm$  standard deviation ( $RSD \leq 5\%$ ,  $n = 3$ ) c) CVs of the catalysts in 1.0 M KOH + 1.0 M ethanol solution. d) Mass and specific activities of the catalysts. Error bars represent  $\pm$  standard deviation ( $RSD \leq 5\%$ ,  $n = 3$ ). e) EIS Nyquist plots of ethanol oxidation on the catalysts in 1.0 M KOH + 1.0 M ethanol solution. Inset: equivalent circuit model f) CO stripping voltammograms of the catalysts in 1.0 M KOH solution at  $50 \text{ mV s}^{-1}$ . g) Chronoamperometry curves. h) Plots for forward oxidation peak current density versus cycle number for EOR. i) Comparison of the electrocatalytic properties of the catalysts. j) Comparison of mass and specific activities with the representative Pd-based catalysts.

Each plot includes a semicircle in the high-frequency range, indicative of a process limited by electron transfer, while a linear segment in the low-frequency range, representing the diffusion-limited processes. Table S4 recorded the fitted EIS data for EOR over the Pdene, FA-Pdene and Pd/C catalysts. The solution resistance ( $R_s$ ), charge transfer resistance ( $R_{ct}$ ), and constant phase element (CPE- $n$ ) values were obtained using an equivalent circuit model (as shown in the inset of Figure 4e). Clearly, FA-Pdene exhibits a lower charge

transfer resistance ( $R_{ct}$ ,  $76.5 \Omega$ ) compared to Pdene ( $R_{ct}$ ,  $85.5 \Omega$ ) and Pd/C ( $R_{ct}$ ,  $580.3 \Omega$ ). The observed reduction in charge transfer resistance ( $R_{ct}$ ) in FA-Pdene highlights the easier and faster charge transfer, as well as more favorable electrocatalytic reaction kinetics.<sup>[9]</sup> This enhancement can be attributed to the Pd–NH<sub>2</sub>–C<sub>60</sub> interaction, which facilitates the electron transfer during the electrochemical EOR process. The  $R_s$  values of the three catalysts are similar, which indicates that the influence of solution resistance on the kinetics



of electrocatalytic EOR over different catalysts can be neglected, and the kinetic differences are mainly determined by the charge transfer process. The kinetics of EOR on FA-Pdene was further analyzed through CV measurements at scanning rates varying from 50 to 200 mV s<sup>-1</sup> in a solution containing 1.0 M KOH + 1.0 M ethanol (Figure S9). The plot derived from these CV curves demonstrates a linear relationship between the current density (*j*) and the square root of the scan rate (*v*<sup>1/2</sup>), indicating that the electrocatalytic EOR for the FA-Pdene catalyst is limited by diffusion.<sup>[37]</sup> In summary, the modification of Pdene with FA molecules promotes the kinetics of EOR and boosts the catalytic activity.

Anti-poisoning performance is crucial for achieving efficient EOR. The tolerance of FA-Pdene to CO-poisoning was investigated through CO-stripping experiments. As illustrated in the CO stripping CVs (Figure 4f), FA-Pdene displays an onset potential (*E*<sub>CO,o</sub>) of -0.36 V and a peak potential of -0.25 V for CO oxidation. These potentials represent a negative shift compared to those observed for Pdene (-0.31 and -0.23 V), and Pd/C (-0.31 and -0.22 V). This indicates that the incorporation of FA effectively enhances the resistance of Pd to CO poisoning, which can be attributed to the electron-deficient nature of the Pdene surface resulting from the electron transfer from Pd to FA. The electron-deficient Pd sites weaken their interaction with the similarly electron-deficient 2 $\pi^*$  antibonding orbitals of CO.<sup>[38]</sup> Consequently, a lower potential is required for the desorption of CO from the Pd sites, leading to the improved resistance to CO poisoning. Moreover, we employed CO poisoning experiments to further investigate the mass activity loss of the catalysts after CO adsorption. As shown in the Figure S10, FA-Pdene exhibited the least mass activity loss after being supplied for CO gas for 5 min, further indicating its superior resistance to CO poisoning. Chronoamperometry (CA) was employed to test the long-term stability of FA-Pdene, Pdene, and Pd/C. From the *j*-*t* curves in Figure 4g, it is evident that all catalysts display a prompt decline in current density during the initial stage of EOR, which is due to the occupation of Pd active sites by carbonaceous poisoning species (e.g., CO<sub>ads</sub>) produced by EOR.<sup>[39]</sup> After 4000 s, FA-Pdene maintains a high current density of 182.5 mA mg<sub>Pd</sub><sup>-1</sup>, while the current densities of Pdene and commercial Pd/C were significantly lower, at 28.7 and 2.5 mA mg<sub>Pd</sub><sup>-1</sup>, respectively. This result indicates the enhanced durability of FA-Pdene. In order to investigate the deactivation mechanism of the catalyst, we test the CVs of Pdene, FA-Pdene, and Pd/C before CA measurements, as well as CVs after regeneration following 4000 s of CA testing. As depicted in Figure S11, FA-Pdene, Pdene, and Pd/C recover respectively 93.2%, 88.9%, and 86.2% of their corresponding original mass activity. The results strongly suggest that the deactivation process is dominated by carbonaceous intermediates poisoning. Therefore, the improvement in durability of FA-Pdene likely arises from the enhanced resistance of the catalytic interface to carbonaceous species, which contributes to the renewal of Pd active sites during the EOR process. Meanwhile, the enhanced stability of FA-Pdene can be verified by CV measurements (Figures 4h and S12). After enduring 500 consecutive CV scans, the mass activity of FA-Pdene retained 30.0% of its initial value,

which is notably higher compared to Pdene (15.0%) and Pd/C (0.4%). The morphological stability of FA-Pdene post EOR (i.e., after 4000 s of *i*-*t* measurement) was examined by TEM images and EDS elemental analysis (Figures S13, S14 and Table S5). The results show that FA-Pdene retains its 2D wrinkled nanosheet structure, and there are negligible changes in the contents of each element before (Table S1) and after (Table S5) the stability test.

To further highlight the distinct advantage of FA, we utilized ethylenediamine (EDA), an organic fatty amine endowed with electron-donating properties, to modify Pdene and evaluated the EOR performance of the material. The successful modification of Pdene by EDA was confirmed through FT-IR and XPS measurements (Figure S15 and Table S4), and the modification did not affect the morphology of Pdene (Figure S16). As demonstrated in the FT-IR spectrum (Figure S15a), the peak located around 3250 cm<sup>-1</sup> is attributed to the absorption corresponding to the N-H stretching mode, and the peaks at 1630 and 1087 cm<sup>-1</sup> are the N-H bending vibration and C-N stretching mode, respectively.<sup>[23]</sup> The C-C, N-H and C-N bonds were also observed in the high-resolution of C 1s and N 1s XPS spectra, respectively (Figure S15d,e). Notably, the XPS spectrum of Pd 3d reveals a negative shift of 0.1 eV in the Pd<sup>0</sup> peak when compared to that of Pdene (Figure S15f), indicating the electron transfer from EDA to Pd, which ultimately leads to an electron-enriched surface on Pd. This is in contrast to the results obtained with FA modification. In addition, the modification of Pdene by planar-structured EDA not only failed to enhance its dispersibility (Figure S1) but also reduced its electrochemically active surfaces (Figure S17a,b). The reduced availability of surface active sites, coupled with unfavorable alterations in the electronic structures, results in a substantial reduction in mass activity (Figure S17c), resistance to CO poisoning (Figure S17d) and stability (Figure S17e,f) compared to the pristine Pdene (Figure 4i). These findings emphasize the advantages of FA, particularly its unique functionality manifested through electronic modulation.

Furthermore, to ascertain the universality of the FA-Pdene catalyst in alcohol oxidation reactions, experiments were conducted for the methanol oxidation reaction (MOR) and ethylene glycol oxidation reaction (EGOR) in alkaline media, using both Pdene and FA-Pdene catalysts for comparison. As depicted in Figures S18 and S19, FA-Pdene shows better activity and stability for MOR (1591.2 mA mg<sub>Pd</sub><sup>-1</sup>) and EGOR (4064.2 mA mg<sub>Pd</sub><sup>-1</sup>), in comparison to Pdene (1162.2 mA mg<sub>Pd</sub><sup>-1</sup> for MOR and 2584.3 mA mg<sub>Pd</sub><sup>-1</sup> for EGOR). The introduction of FA results in a well-performing catalytic surface, enhancing the alcohol oxidation properties of Pdene.

### Electro-Oxidation Mechanism on FA-Pdene

The electrochemical EOR involves spontaneous dissociation of ethanol at lower potentials and oxidation of ethanol at higher potentials. In the EOR process, there are usually two competing oxidation pathways, namely C1 (C-C bonds breaking) and C2 (without the breaking of C-C bonds). The

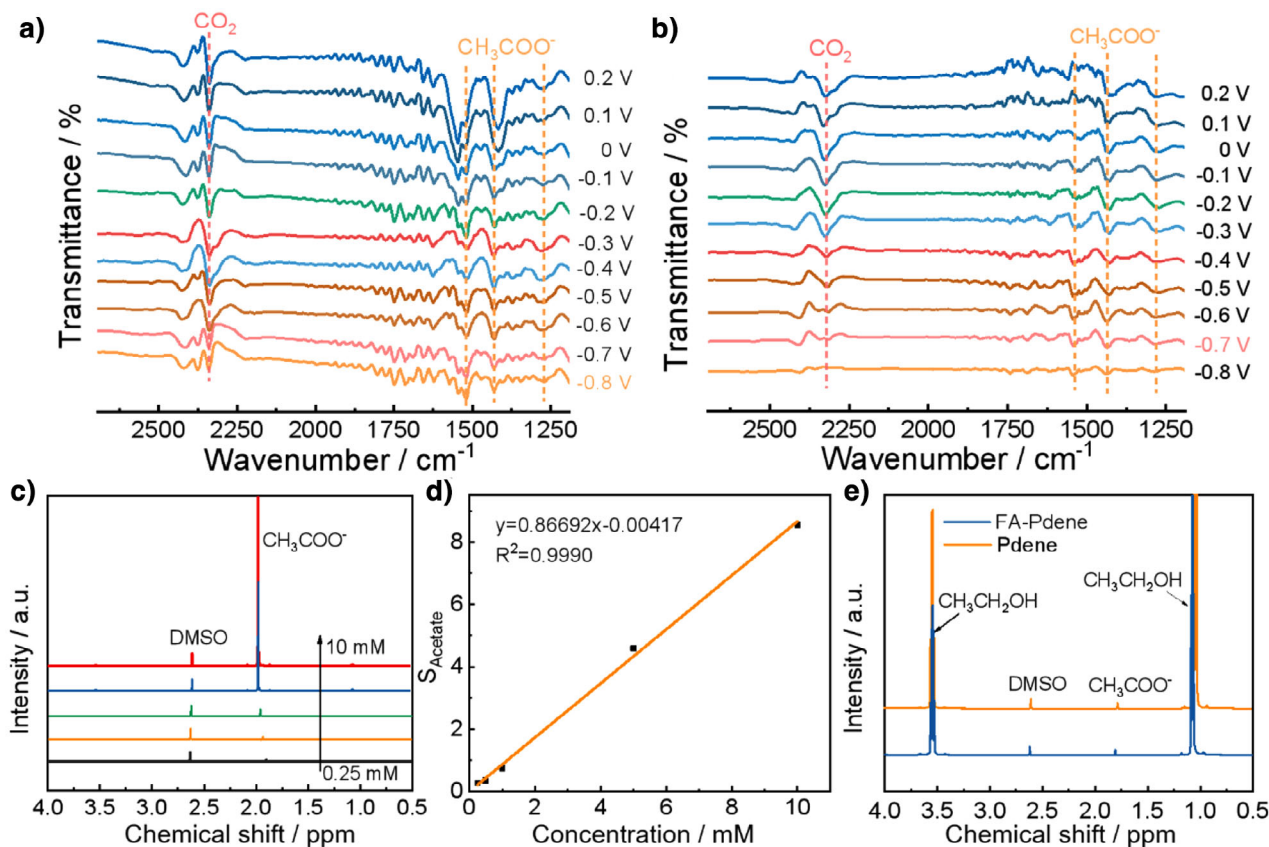


**Figure 5.** In situ ATR-FTIR spectra for ethanol decomposition on a) FA-Pdene and b) Pdene in 1 M KOH + 1.0 M ethanol solution measured at different potential varying from  $-0.8$  to  $0.2$  V versus SCE at an interval of  $0.1$  V. c)  $^1\text{H}$  NMR results and d) the corresponding standard curves for different concentrations of acetic acid. e)  $^1\text{H}$  NMR spectra of the electrolytes obtained by running chronoamperometry at  $-0.34$  V versus SCE for an electric charge of  $50$  C on the Pdene and FA-Pdene catalysts.

C1 pathway involves the complete oxidation of ethanol to CO<sub>2</sub> through a 12-electron ( $12e^-$ ) process, and the C2 pathway involves the incomplete oxidation of ethanol, resulting in the formation of acetate through a 4-electron ( $4e^-$ ) process. In-situ attenuated total reflection Fourier transform infrared spectroscopy (ATR-FTIR) of ethanol oxidation on the FA-Pdene and Pdene electrodes was conducted and the results are presented in Figure 5a,b.

By collecting the evanescent wave signals, the evolution of reaction intermediates during the ethanol oxidation reaction was observed. Notably, the characteristic absorption band at  $2337\text{ cm}^{-1}$  for the FA-Pdene electrode and  $2321\text{ cm}^{-1}$  for the Pdene electrode correspond to the production of CO<sub>2</sub>,<sup>[40]</sup> a product of the complete oxidation of ethanol. This observation indicates the presence of the C1 pathway in both cases. Additionally, the characteristic absorption bands associated with the acetate ion (CH<sub>3</sub>COO<sup>-</sup>) are identified at  $1519$ ,  $1430$ , and  $1272\text{ cm}^{-1}$  for the FA-Pdene electrode and  $1538$ ,  $1436$ , and  $1280\text{ cm}^{-1}$  for the Pdene electrode, respectively.<sup>[40]</sup> These findings agree with the C2 pathway. It can be observed that FA-Pdene demonstrates higher peak intensities for C1 and C2 products compared to Pdene, suggesting a higher catalytic efficiency during the EOR process.<sup>[41]</sup> Furthermore, it is noteworthy that the vibrational signal corresponding to CO<sub>2</sub> on the FA-Pdene electrode

appears at  $-0.8$  V, which is more negative compared to  $-0.7$  V on the Pdene electrode, implying that the reaction energy barrier for the C1 pathway on FA-Pdene is lower than that for Pdene. Therefore, FA-Pdene exhibits advantages in efficiently catalyzing the cleavage of C–C bonds during the EOR process, thereby promoting the C1 pathway. This can be verified by the  $^1\text{H}$  nuclear magnetic resonance (NMR) measurements as depicted in Figure 5c–e. Based on the quantity of CH<sub>3</sub>COOK present in both cases depicted in Figure 5e, the C1 efficiency of FA-Pdene has been determined to be  $30.1\%$ , which represents a  $38.0\%$  increase compared to the  $21.8\%$  efficiency of Pdene.

### DFT Analysis

Density functional theory (DFT) calculations were performed to reveal the impacts of surface FA and EDA molecules on the electrocatalytic EOR process. The optimized atomic structure models of FA-Pdene (The functionalization positions of NH<sub>2</sub> and OH groups on C<sub>60</sub> were arbitrarily selected) and EDA-Pdene used for calculations are illustrated in Figure 6a,b. In the model for FA-Pdene, the diameter of FA was approximately  $1.2\text{ nm}$ , which is consistent with the AFM test results. The FA and EDA molecules are bound to the



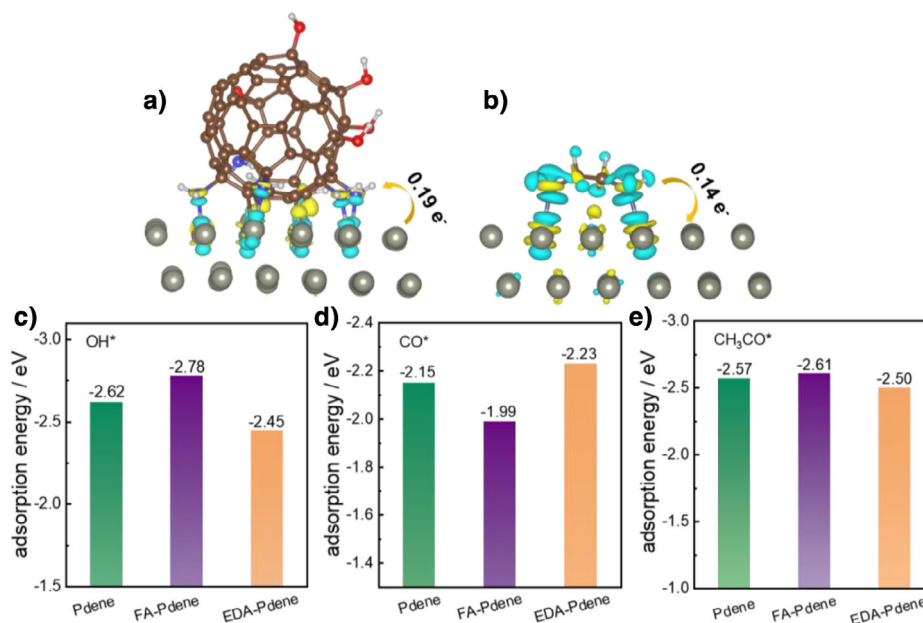


**Figure 6.** DFT calculation results for the electron density difference maps for a) FA-Pdene and b) EDA-Pdene. c) The calculated OH\*, d) CO\*, and e) CH<sub>3</sub>CO\* adsorption energy on Pdene, FA-Pdene, and EDA-Pdene surfaces.

surface of Pdene through the interaction between the -NH<sub>2</sub> groups and the Pd atoms. As depicted in Figure 6a,b, the electron density difference maps reveal distinct disparity of the charge distribution between FA-Pdene and EDA-Pdene. In the case of FA-Pdene, the map shows electron enrichment (indicated by yellow) at the base of the FA molecule and electron depletion (indicated by blue) at the upper surface of Pdene, indicating electron transfer from the surface of Pdene to the FA molecule. The electron deficiency on the surface of Pdene can produce an extra positive potential, which favors the oxidation of ethanol.<sup>[42]</sup> In addition, as the 2 $\pi^*$  orbital of CO is also electron-deficient, the adsorption of CO onto FA-Pdene is decreased. Consequently, FA-Pdene exhibits enhanced resistance to CO poisoning, as evidenced by the negative shift in both the onset and peak potentials during CO stripping (Figure 4f). On the contrary, EDA transfers electron density to the Pdene surface (Figure 6b), thereby enhancing the affinity of Pdene for CO and diminishing its resistance to poisoning.

In addition, the adsorption energies of key reaction intermediates involved in the EOR process, namely OH\*, CO\*, and CH<sub>3</sub>CO\* were analyzed on the surface of Pdene, FA-Pdene and EDA-Pdene (Figure S20). As displayed in Figure 6c, compared with Pdene ( $E_{ad} = -2.62$  eV) and EDA-Pdene ( $E_{ad} = -2.45$  eV), FA-Pdene exhibits the strongest adsorption for OH\* ( $E_{ad} = -2.78$  eV). This heightened adsorption can be attributed to the generation of hydrogen bonds between the -NH<sub>2</sub>/OH groups and OH\*.<sup>[43]</sup> The preferential adsorption of OH\* on FA-Pdene facilitates the oxidation and removal of CO. Even more advantageous, FA-Pdene exhibits the lowest adsorption capacity for CO\* in comparison to Pdene and EDA-Pdene (Figure 6d), highlighting its enhanced resistance to CO poisoning. This advantageous property is attributed to the formation of an electron-deficient

Pd surface on FA-Pdene. In the context of the EOR process, it is commonly accepted that the selectivity between the C1 and C2 pathways depends on whether CH<sub>3</sub>CO\* undergoes dehydrogenation to form CH<sub>2</sub>CO\* for subsequent dissociation or oxidation to produce CH<sub>3</sub>COOH\*. Specifically, enhancing the adsorption of CH<sub>3</sub>CO\* can promote its dissociation, whereas weakening its adsorption favors the removal of CH<sub>3</sub>CO\* in its C2 form without undergoing C–C dissociation. After introducing FA onto Pdene, the adsorption of CH<sub>3</sub>CO\* is enhanced (Figure 6e), which favors the C1 pathway.

## Conclusions

In summary, the hydrophilic spherical FA molecules with electron-withdrawing properties not only effectively disperse Pdene, it also affects the electronics of the Pd active sites. Thus, the addition of FA boosts the availability of surface sites of Pdene and optimizes the electronic structure of the Pd sites, thereby enabling FA-Pdene to have enhanced performance for EOR in terms of activity, stability, and C1 pathway selectivity. Surface modification of metal catalysts through the use of molecules with distinct electronic and spatial effects offers promising opportunities for creating highly effective catalytic interfaces tailored for specific reactions. Our work demonstrates that fullerene molecules are poised to play an increasingly significant and diverse role in the design of high-performance catalysts.

## Acknowledgements

The authors appreciate the financial support from the National Natural Science Foundation of China (22071070,

22272006) and the Open Project of State Key Laboratory of Supramolecular Structure and Materials (sklssm2024021). LE wishes to thank the Institut Català d'Investigació Química (ICIQ) for their support. Part of the computation is completed in the HPC Platform of Huazhong University of Science and Technology.

## Conflict of Interests

The authors declare no conflict of interest.

## Data Availability Statement

The data that support the findings of this study are available from the Supplementary Information and/or the corresponding author upon reasonable request.

**Keywords:** Electrocatalysis • Ethanol oxidation reaction • Fullerene • Pd metallene • Surface modification

- [1] I. E. L. Stephens, J. Rossmeisl, I. Chorkendorff, *Science* **2016**, 354, 1378–1379.
- [2] A. Chen, C. Ostrom, *Chem. Rev.* **2015**, 115, 11999–12044.
- [3] Y. Ge, Z. Huang, C. Ling, B. Chen, G. Liu, M. Zhou, J. Liu, X. Zhang, H. Cheng, G. Liu, Y. Du, C.-J. Sun, C. Tan, J. Huang, P. Yin, Z. Fan, Y. Chen, N. Yang, H. Zhang, *J. Am. Chem. Soc.* **2020**, 142, 18971–18980.
- [4] M. Luo, Z. Zhao, Y. Zhang, Y. Sun, Y. Xing, F. Lv, Y. Yang, X. Zhang, S. Hwang, Y. Qin, J.-Y. Ma, F. Lin, D. Su, G. Lu, S. Guo, *Nature* **2019**, 574, 81–85.
- [5] M. Luo, Y. Yang, Y. Sun, Y. Qin, C. Li, Y. Li, M. Li, S. Zhang, D. Su, S. Guo, *Mater. Today*, **2019**, 23, 45–56.
- [6] Z.-H. Yuan, T.-J. Wang, B. Sun, Q.-L. Hong, X. Ai, S.-N. Li, J. Bai, Y. Chen, *Appl. Catal. B Environ.* **2025**, 366, 125041.
- [7] P. Prabhu, J.-M. Lee, *Chem. Soc. Rev.* **2021**, 50, 6700–6719.
- [8] J. Fan, J. Wu, X. Cui, L. Gu, Q. Zhang, F. Meng, B.-H. Lei, D. J. Singh, W. Zheng, *J. Am. Chem. Soc.* **2020**, 142, 3645–3651.
- [9] K. Deng, T. Zhou, Q. Mao, S. Wang, Z. Wang, Y. Xu, X. Li, H. Wang, L. Wang, *Adv. Mater.* **2022**, 34, 2110680.
- [10] W. Zhong, Q. L. Hong, X. Ai, C. Zhang, F. M. Li, X. F. Li, Y. Chen, *Adv. Mater.* **2024**, 36.
- [11] Z.-X. Ge, T.-J. Wang, Y. Ding, S.-B. Yin, F.-M. Li, P. Chen, Y. Chen, *Adv. Energy Mater.* **2022**, 12, 2103916.
- [12] H. Yu, T. Zhou, Z. Wang, Y. Xu, X. Li, L. Wang, H. Wang, *Angew. Chem. Int. Ed.* **2021**, 60, 12027–12031.
- [13] F. Lin, F. Lv, Q. Zhang, H. Luo, K. Wang, J. Zhou, W. Zhang, W. Zhang, D. Wang, L. Gu, S. Guo, *Adv. Mater.* **2022**, 34, 2202084.
- [14] B. Sun, W. Zhong, X. Ai, C. Zhang, F.-M. Li, Y. Chen, *Energy Environ. Sci.* **2024**, 17, 2219–2227.
- [15] C. A. Schoenbaum, D. K. Schwartz, J. W. Medlin, *Acc. Chem. Res.* **2014**, 47, 1438–1445.
- [16] R. Du, J. Wang, Y. Wang, R. Hübner, X. Fan, I. Senkovska, Y. Hu, S. Kaskel, A. Eychmüller, *Nat. Commun.* **2020**, 11, 1590.
- [17] J. Zheng, L. Huang, C.-H. Cui, Z.-C. Chen, X.-F. Liu, X. Duan, X.-Y. Cao, T.-Z. Yang, H. Zhu, K. Shi, P. Du, S.-W. Ying, C.-F. Zhu, Y.-G. Yao, G.-C. Guo, Y. Yuan, S.-Y. Xie, L.-S. Zheng, *Science* **2022**, 376, 288–292.
- [18] Y. Zhang, X. Peng, H.-R. Tian, B. Yang, Z.-C. Chen, J. Li, T. Zhang, M. Zhang, X. Liang, Z. Yu, Y. Zhou, L. Zheng, X. Wang, J.-W. Zheng, Y. Tang, C.-t. Au, L. Jiang, S.-Y. Xie, *Nat. Chem.* **2024**, 16, 1781–1787.
- [19] R. Zhang, Y. Li, X. Zhou, A. Yu, Q. Huang, T. Xu, L. Zhu, P. Peng, S. Song, L. Echegoyen, F.-F. Li, *Nat. Commun.* **2023**, 14, 2460.
- [20] W. Yang, Q. Huang, Y. Yan, Y. Li, T. Xu, A. Yu, Y. Zhao, P. Peng, Y. Wang, L. Echegoyen, F.-F. Li, *Angew. Chem. Int. Ed.* **2025**, 64, e202414149.
- [21] Y. Li, T. Xu, Q. Huang, L. Zhu, Y. Yan, P. Peng, F.-F. Li, *ACS Catal.* **2023**, 13, 7597–7605.
- [22] J. Chen, M. Aliasgar, F. B. Zamudio, T. Zhang, Y. Zhao, X. Lian, L. Wen, H. Yang, W. Sun, S. M. Kozlov, W. Chen, L. Wang, *Nat. Commun.* **2023**, 14, 1711.
- [23] T. Cao, P. Huang, K. Zhang, Z. Sun, K. Zhu, L. Yuan, K. Chen, N. Chen, Y. Li, *J. Mater. Chem. A* **2018**, 6, 3435–3443.
- [24] V. V. Sharoyko, S. V. Ageev, A. A. Meshcheriakov, A. V. Akentiev, B. A. Noskov, I. T. Rakipov, N. A. Charykov, N. A. Kulenova, B. K. Shaimardanova, N. E. Podolsky, K. N. Semenov, *J. Mol. Liq.* **2020**, 311, 113360.
- [25] Z. You, Z. Zhao, Q. Zhang, C. Zhang, X. Long, D. Li, Y. Xia, *Adv. Funct. Mater.* **2023**, 33, 2210877.
- [26] J. Zhang, F. Lv, Z. Li, G. Jiang, M. Tan, M. Yuan, Q. Zhang, Y. Cao, H. Zheng, L. Zhang, C. Tang, W. Fu, C. Liu, K. Liu, L. Gu, J. Jiang, G. Zhang, S. Guo, *Adv. Mater.* **2022**, 34, 2105276.
- [27] S. Guo, S. Dong, E. Wang, *Energy Environ. Sci.* **2010**, 3, 1307.
- [28] X. Zhou, S. Liu, H. Teng, K. Ma, W. Miao, X. Cui, X. Zhou, L. Jiang, *Small* **2024**, 20, 2408373.
- [29] C. Liu, Y. Shen, J. Zhang, G. Li, X. Zheng, X. Han, L. Xu, S. Zhu, Y. Chen, Y. Deng, W. Hu, *Adv. Energy Mater.* **2022**, 12, 2103505.
- [30] S. Li, J. Shu, S. Ma, H. Yang, J. Jin, X. Zhang, R. Jin, *Appl. Catal. B Environ.* **2021**, 280, 119464.
- [31] Q. Guo, J. Dou, X. Yang, Z. Jiang, H. Wang, Y. Liu, H. Xie, X. Li, *Adv. Funct. Mater.* **2024**, 2413937.
- [32] T. Zeng, X. Meng, S. Sun, M. Ling, C. Zhang, W. Yuan, D. Cao, M. Niu, L. Y. Zhang, C. M. Li, *Small Methods* **2023**, 7, 2300791.
- [33] X. Lao, X. Zhang, T. Sun, A. Fu, Y. Zhang, Z. Li, L. Yang, C. Chen, X. Liao, J. Wang, W. Ye, P. Guo, *Chem. Mater.* **2024**, 36, 2124–2137.
- [34] Y. Wang, M. Li, Z. Yang, W. Lai, J. Ge, M. Shao, Y. Xiang, X. Chen, H. Huang, *Mater. Horiz.* **2023**, 10, 1416–1424.
- [35] A. Pei, G. Li, L. Zhu, Z. Huang, J. Ye, Y.-C. Chang, S. M. Osman, C.-W. Pao, Q. Gao, B. H. Chen, R. Luque, *Adv. Funct. Mater.* **2022**, 32, 2208587.
- [36] X. Lao, X. Liao, C. Chen, J. Wang, L. Yang, Z. Li, J.-W. Ma, A. Fu, H. Gao, P. Guo, *Angew. Chem. Int. Ed.* **2023**, 62, e202304510.
- [37] Y. Wang, M. Zheng, Y. Li, L. Zhu, H. Li, Q. Wang, H. Zhao, J. Zhang, Y. Dong, Y. Zhu, *Adv. Powder Mater.* **2024**, 3, 100244.
- [38] G. Chen, C. Xu, X. Huang, J. Ye, L. Gu, G. Li, Z. Tang, B. Wu, H. Yang, Z. Zhao, Z. Zhou, G. Fu, N. Zheng, *Nat. Mater.* **2016**, 15, 564–569.
- [39] J. Liu, Q. Wang, T. Li, Y. Wang, H. Li, A. Cabot, *Nano Res.* **2023**, 16, 2041–2048.
- [40] X. Huang, J. Feng, S. Hu, B. Xu, M. Hao, X. Liu, Y. Wen, D. Su, Y. Ji, Y. Li, Y. Li, Y. Huang, T.-S. Chan, Z. Hu, N. Tian, Q. Shao, X. Huang, *Nat. Nanotechnol.* **2024**, 19, 1306–1315.
- [41] X. Tan, C. Wang, J. Wang, P. Wang, Y. Xiao, Y. Guo, J. Chen, W. He, Y. Li, H. Cui, C. Wang, *Adv. Sci.* **2024**, 11, 2409109.
- [42] S. Zhang, Y. Guo, L.-H. Zhang, Z. Feng, B. Zhang, Y. Wang, F. Yu, *J. Energy Chem.* **2024**, 98, 524–530.
- [43] Y. Qiu, J. Fan, J. Wu, W. Lu, S. Wang, D. Wang, X. Ge, X. Zhao, W. Zhang, W. Zheng, X. Cui, *Nano Lett.* **2023**, 23, 9555–9562.

Manuscript received: March 16, 2025

Revised manuscript received: May 23, 2025

Accepted manuscript online: June 04, 2025

Version of record online: ■■■■■

## Research Article

## Electrocatalysis

S. Xie, J. Fu, Q. Huang, W. Yang, A. Yu,  
Y. Yan, Z. Li, P. Peng, Y. Yin, H. Wang,  
L. Echegoyen, F.-F. Li\* — e202506044

Electronic Modulation and Active Site  
Exposure Using C<sub>60</sub> Fullerenolamine  
Enable High-Performance Alcohol  
Oxidation on Pd Metallene Catalysts

Through Pd-NH<sub>2</sub> coordination bonding, C<sub>60</sub> fullerolamine (FA) was successfully anchored onto the Pd metallene (Pdene) surface. This surface functionalization induces an electron-deficient state in Pd through charge redistribution while simultaneously enhancing the electrochemical active surface area. The resulting electron-deficient Pd sites demonstrate optimized adsorption behavior toward ethanol oxidation intermediates. These synergistic effects endow FA-Pdene to exhibit enhanced mass activity and specific activity for ethanol oxidation compared to Pdene.

